Materials Advances

Accepted Manuscript

This article can be cited before page numbers have been issued, to do this please use: H. U. Rehman, H. Khan, Z. Abbasi, L. Ben Tahar, R. A. Khan, A. Waseem and A. J. Shaikh, *Mater. Adv.*, 2025, DOI: 10.1039/D5MA00846H.

View Article Online
DOI: 10.1039/D5MA00846H

DLS based Optimization of ZnS-CoS Nanoparticles with Enhanced Energy and Power Density for Supercapacitor Applications and Validation by AI Models

Hafeez Ur Rehman[1], Hamza Khan[1], Zeeshan Abbasi[1,2], Lotfi Ben Tahar[3], Rafaqat Ali Khan[1], Amir Waseem[4], and Ahson Jabbar Shaikh[1]*

[1] Department of Chemistry, COMSATS University Islamabad - Abbottabad Campus, Abbottabad - 22060, KPK, Pakistan

[2] National Synchrotron Radiation Laboratory, University of Science and Technology of China, Hefei, Anhui - 230029, China

[3] Department of Chemistry, College of Science, Northern Border University, P.O. Box 1231, Arar - 91431, Saudi Arabia.

[4] Department of Chemistry, Quaid-i-Azam University Islamabad, Islamabad - 45320, Pakistan

*** Corresponding author e-mail (Dr. Ahson J. Shaikh): ahson@cuiatd.edu.pk ahsonjabbar@hotmail.com**

Keywords: Supercapacitors; Machine learning; Stacking regression model; Tree-based Pipeline Optimization Tool; Capacitance prediction

Abstract

Zinc cobalt sulfide (ZnS-CoS) nanoparticles have emerged as promising electrode materials for supercapacitors due to their excellent electrochemical properties. However, achieving both high energy density and power density remains a challenge due to particle agglomeration and instability. In this work, dynamic light scattering based optimization of ZnS-CoS nanoparticles is carried out by adjusting synthetic parameters including temperature, pH, reagent addition rate, and stabilizer concentration, resulting in significantly smaller particle sizes and improved stability. The optimized ZnS-CoS nanoparticles based electrodes exhibited an exceptional specific capacitance of 1156 F/g, an energy density of 194 Wh/kg, and a power density of 7260 W/kg, which are significantly higher than literature-reported values. Electrochemical impedance spectroscopy (EIS) confirmed lower charge transfer resistance (35.88 Ω), indicating faster ion transport and enhanced conductivity. Moreover, the optimized ZnS-CoS electrodes demonstrated remarkable cyclic stability, retaining 93.87% capacitance after 10,000 cycles. The charge transfer mechanism has been understood by computational studies and four

View Article Online
DOI: 10.1039/D5MA00846H

different machine learning models including stacking regressor, TPOT, ANN, and RSM models are applied to verify the experimental specific capacitance of ZnS. The accuracy of models performance is best for stacked regression model followed by ANN, TPOT, and RSM models respectively. These results highlight the critical role of nanoparticle size optimization in enhancing electrochemical performance and establish DLS-optimized ZnS-CoS as a superior candidate for next-generation supercapacitors.

1 Introduction

The transition from fossil fuels to sustainable energy sources has intensified research on efficient energy storage technologies. Among various energy storage devices [1, 2], supercapacitors (SCs) have gained attention due to their high-power density, fast charge-discharge rates, and long cycle life application [3-6]. SCs can be considered ideal candidates for hybrid electric vehicles, reserve storage systems, defense systems, high-energy industrialization systems, and data security for computer and mobile phones [7, 8]. Supercapacitors are often hindered by low energy density, necessitating the development of advanced electrode materials [5, 9].

Transition metal sulfides (TMSs) have emerged as promising candidates for SC electrodes due to their low cost, high electrical conductivity, multiple oxidation states, superior redox activity, and excellent specific capacitance [10-14]. Among TMSs, zinc sulfides and cobalt sulfides stand out due to their high theoretical capacitance, cost-effectiveness, and eco-friendly nature [15-17]. However, pure ZnS and CoS suffer from poor specific capacitance and significant agglomeration [18, 19]. To address this challenge, mixed ZnS-CoS nanoparticles have been explored, leveraging the synergistic effect of Zn and Co to enhance electrical conductivity, stability, and electrochemical performance [20]. The combination of Zn and Co in a sulfide matrix enhances electrochemical activity, conductivity, and cycling stability, making them highly efficient for energy storage applications. ZnS-CoS offers a balance between high specific capacitance and good electrical conductivity, also outperforming many metal oxides and carbon-based materials in energy density.

Synthesis methods are important tools for determining the final structure and characteristics of resulting materials. To date, various methods are reported for the synthesis of pure and mixed TMSs, including precipitation [6, 21-23] hydro/solvothermal [24], electrodeposition [25] and self-template methods [25] etc. Due to the ease of handling, scalability, uniform mixing at the nano level, control of particle size and shape, precipitation is considered as an effective method for the synthesis of nanoparticles [26-28].

View Article Online
DOI: 10.1039/D5MA00846H

Although a variety of work has been done on mixed metal sulfide nanoparticles, very limited work has been done for controlling the size and stability of mixed transition metal sulfide nanoparticles. Optimization of nanoparticles involves the systematic adjustment of various parameters to enhance their properties and performance for specific use. The parameters that can be altered are concentration of constituent sulfides, pH, temperature, reagent addition rate and stabilizer concentration etc. [29, 30]. This results in control in size, shape, composition, and surface chemistry of the resulting nanoparticles. Furthermore, the interactions between nanoparticles and their surroundings can also be analyzed to better understand the impact of their performance [31, 32].

In the last few decades, machine learning approaches have been broadly used in material science to support the discovery of new materials and to predict their performance with accuracy [33]. Machine learning technology accelerates the development and analysis of energy materials, improves accuracy, and reduces research time [34]. Key supercapacitor performance metrics, including specific capacitance [35], power density, energy density [36], and remaining useful life [37], can be predicted using machine learning models. Both modeling-based forecasting techniques and data-driven methodologies can be used to produce these predictions, leading to more precise performance evaluation and productive material optimization.

We believe that particle size and morphology control [38] is an effective strategy for improving the electrochemical performance of TMS-based electrode materials. Over the years, significant efforts have been devoted to exploring the applications of TMS as electrode materials. However, to the best of our knowledge, no strategies have been defined yet to further improve the specific capacitance, power density, energy density, and other parameters of already good-performing materials. In the present study, we trained a stacking regressor and TPOT machine learning models and then successfully applied them to verify the specific capacitance calculated experimentally.

Although ANN and RSM machine learning models are frequently used in the synthesis and optimization of nanoparticles, our work presents a distinct novelty because specific capacitance prediction has mostly been documented for carbon-based [39-41] and for metal oxide-based nanoparticles [42, 43]. To the best of our knowledge, specific capacitance of metal sulfides has not been predicted yet. Additionally, we predict specific capacitance at various scan rates, which are not documented in the literature. Although machine learning models are significant tools but they face limitations such as overfitting, high computational demand, and limited

View Article Online
DOI: 10.1039/D5MA00846H

interpretability [44]. In the present work, we handle these issues by using linearized data and advanced machine learning (ML) approaches to obtain accurate and robust predictions.

2 Materials and Methods

Zinc acetate, sodium sulfide (Na_2S), cobalt acetate hexahydrate, and polyvinyl alcohol were used in the experiments, which were purchased from Dae-Jung Chemicals and Metals Co., Ltd., Republic of Korea. All the solvents and reagents were used exactly as supplied; no further purification was made. 0.1 M stock solution of zinc acetate and cobalt acetate were prepared. 0.2 M stock solution of sodium sulfide was prepared. 1% solution of polyvinyl alcohol was prepared by dissolving 1 g of PVA in 100 mL of distilled water and stirring at 1500 rpm for 30 minutes at 50°C.

2.1 Synthesis of ZnS NPs

In 50 mL conical flask, 10 mL of PVA solution and 10 mL of 0.1 M zinc acetate were added. The flask was then heated to 40°C and stirred at 1300 rpm using a magnetic stirrer on a hot plate. 20 mL of 0.2 M $Na_2S{\cdot}3H_2O$ solution was rapidly added to this solution, while the temperature was maintained at 40°C. White precipitates were formed after 90 minutes of stirring. The resulting zinc sulfide nanoparticles solution was then centrifuged at 8000 rpm for 20 minutes. The precipitates were washed three times with distilled water and kept for 12 hours at 110°C in the oven for complete drying.

2.2 Synthesis of CoS NPs

10 mL of 0.1 M cobalt acetate solution was added to 10 mL of 1% PVA solution in a 50 mL conical flask and was placed on a hot plate magnetic stirrer at 40°C and stirred at 1300 rpm. 20 mL of a 0.2 M $Na_2S{\cdot}3H_2O$ solution was quickly added to this solution while the temperature was maintained at 40°C with constant stirring. After 90 minutes of stirring, black precipitates of cobalt sulfide were observed. After centrifuging the prepared solution at 8000 rpm, the precipitates were washed three times with distilled water and placed in an oven at 110 °C for drying.

2.3 Synthesis of ZnS-CoS Nanoparticles

ZnS-CoS (50:50) mixed metal sulfide nanoparticles were synthesized using the simplest co-precipitation process. Conical flask containing 10 mL of PVA solution and 5 mL of each 0.1 M zinc acetate and cobalt acetate solution was placed on a hot plate magnetic stirrer at 40°C and stirred at 1300 rpm. 20 mL of 0.2 M $Na_2S{\cdot}3H_2O$ solution was quickly added to this mixture, while temperature was maintained at 40°C with constant stirring at 1300 rpm. After 90 minutes,

View Article Online
DOI: 10.1039/D5MA00846H

the black solution for mixed cobalt sulfide and zinc sulfide was produced. The prepared solution was centrifuged and washed three times with distilled water and then kept in the oven at 110°C for further drying.

2.4 Concentration-Dependent Synthesis of ZnS-CoS Nanoparticles

The co-precipitation method discussed above was used to synthesize three different kinds of mixed ZnS-CoS nanoparticles (25:75), (50:50), and (75:25) using different amounts of zinc acetate and cobalt acetate, i.e., 2.5 mL: 7.5 mL, 5 mL: 5 mL, and 7.5 mL: 2.5 mL, respectively. Depending on the stability, polydispersity index, particle size, and optical properties, further optimization was carried out on 50:50 mixed metal sulfide nanoparticles.

2.5 Temperature-Dependent Synthesis of ZnS-CoS Nanoparticles

The above method was used for synthesizing mixed ZnS-CoS nanoparticles at various temperatures (20°C, 40°C, 60°C, and 80°C). Hydrodynamic size, PDI, and stability are all greatly affected by temperature. Based on the results, further optimization was carried out at 80°C.

2.6 pH-Dependent Synthesis of ZnS-CoS Nanoparticles

First, the pH of the solution containing 1% PVA (10 mL), 0.2 M $Na_2S{\cdot}3H_2O$ (20 mL), and 0.1 M zinc and cobalt acetate solution (5 mL + 5 mL) was measured and found to be 11.5. pH levels of 3, 5, 7, 9, 11, and 13 were adjusted by adding 0.1 M HCl or NaOH while maintaining the ideal temperature of 80°C and keeping 1:1 ratio of metal salts. The synthesis procedure was followed as mentioned above. Based on the smaller size and reasonable stability, further improvements were made at pH 7.

2.7 Reagent Rate-Dependent Synthesis of ZnS-CoS Nanoparticles at Room Temperature

At the ideal condition of 1:1 ratio of salts, 80°C, and pH 7, the effect of the sulfide source ($Na_2S{\cdot}3H_2O$) addition rate on mixed metal sulfide nanoparticles was investigated. With the above-described procedure and then gradually adding sodium sulfide over a range of time intervals (5, 10, 15, and 20 minutes), the best results were revealed at quick addition of sulfide source.

2.8 Stabilizer-Dependent Synthesis of mixed ZnS-CoS Nanoparticles

The capping agent acts as a stabilizing and size-controlling component. The procedure described above was followed to synthesize mixed metal sulfide nanoparticles without PVA and with varying amounts of PVA concentrations of 0.5%, 1%, and 2% under optimized

View Article Online
DOI: 10.1039/D5MA00846H

conditions such 1:1 ratio of salts, pH 7, 80°C, and quick addition of reagent. The optimal concentration of PVA was found to be 2%.

2.9 Electrode Fabrication

Active material, carbon black (or graphite), and Nafion were mixed in an 8:1:1 weight ratio. All of the materials were combined using a pestle and mortar, and the resulting thick slurry was obtained by adding 10% Nafion drop by drop. Ni foam was used as the substrate for the electrode fabrication process; Ni foam was weighed before electrode material deposition, and electrode material was then transferred on Ni foam so that a uniform layer was formed after that nickel foam was dried in a vacuum oven at 60℃. The active mass of the electrode that is deposited on the Ni foam is calculated by the weight difference between the electrodes before and after depositing and drying.

2.10 Electrochemical Studies

ZIVE SP1 was used for the various electrochemical analyses, including CV, GCD, and EIS. 1M KOH was used as an electrolyte. Pt wire and silver/silver chloride electrodes were used as counter and reference electrodes, respectively, while nickel foam was used as the working electrode. CV and GCD experiments were conducted in the potential window of -0.4 to 0.6V. EIS experiment was carried out in the frequency range of 0.01 Hz to 100 kHz.

Specific capacitance is calculated from CV curve by using equation given below

$$c_{\mathrm{P}} = A/(2mvdV) \qquad 1$$

Where C_p is the specific capacitance, A is the integrated area m is mass of electrode materials ν is the scan rate, and dv is the difference in the potential window. Window potential is generally measured in Volts [45, 46].

The following equation is used to calculate specific capacitance from GCD curve

$$C_S = I_m \times \Delta t/\Delta V \qquad 2$$

Where ΔV stands for potential window. Δt is the discharging time while I_m is current density. Energy density E and power density P are determined by using following equation

$$E = c_s \times \Delta v/7.2 \qquad 3$$

$$P = 3600 \times E/\Delta t \qquad 4$$

2.11 Machine Learning Model Development

All machine learning model development, training, and evaluation were conducted using the Python programming language (version 3.9). The neural network models were implemented

View Article Online
DOI: 10.1039/D5MA00846H

using the TensorFlow library (version 2.x), with Keras APIs for model construction and training. Data preprocessing tasks, such as feature scaling and train-test splitting, were performed using scikit-learn (version 0.24), specifically employing the StandardScaler, train_test_split, and performance metric functions such as mean squared error (MSE) and R^2 score. Visualization of model performance (scatter plots of actual vs. predicted values) was performed using Matplotlib (version 3.4). Tabular data manipulation and input data reading from Excel files were handled using pandas (version 1.3). The experimental data was imported from a Microsoft Excel (XLSX) file. Each scan rate dataset was trained using an independent feed-forward neural network (ANN) consisting of two hidden layers (64 neurons each, ReLU activation), and a single output neuron for regression. Models were compiled using the Adam optimizer and the mean squared error (MSE) loss function. Model training was performed over 100 epochs with a batch size of 16.

In this study, feed-forward artificial neural networks (ANNs) that are well-established for regression problems involving complex non-linear relationships between input variables and the target output were used. Operating parameters like scan rate have a significant impact on the specific capacitance of electrochemical materials, and feed-forward ANNs are the best choice to learn these non-linear dependencies than conventional linear models. Two hidden layers were chosen to maintain a balance between computational simplicity and predictive accuracy. Our initial trials revealed that one hidden layer was not sufficient to fully capture the non-linear response, and that more than two layers increased the risk of overfitting. 64 neurons were assigned to each hidden layer, which provides sufficient function approximation capacity while maintaining a manageable model complexity. This design choice aligns with materials modeling, which is used for small-to-medium networks to avoid overparameterization when working with small experimental datasets.

The hidden layers used the ReLU activation function, which is commonly known as the default activation, is computationally efficient, and avoids vanishing gradient issues used in modern ANN applications. Since specific capacitance is a continuous-valued property and the task is a regression problem, a single linear output neuron was used. The Adam optimizer, a popular algorithm that adaptively modifies learning rates and generally ensures faster convergence than conventional stochastic gradient descent, was used to train the model. Since the mean squared error (MSE) loss function is the default option for regression models and assess larger deviations more significantly, it was selected to accurately predict capacitance values.

Training was carried out with a batch size of 16 over 100 epochs. These values were selected after initial testing, which demonstrated that this configuration offered a favorable trade-off between convergence speed, training stability, and computational efficiency. For this relatively small dataset, smaller batch sizes give more stable weight updates, but a greater number of epochs did not significantly improve validation metrics The scan rate was selected as the input feature because it is a physically valuable predictor and has a strong correlation with specific capacitance, as observed in experiments. To ensure that all values were on a similar scale and to enhance numerical stability during optimization, the data were standardized using scikit-learn's StandardScaler before training. By examining the trained ANN models using mean squared error and coefficient of determination (R^2), the accuracy of these parameters was verified. Both metrics indicated that the network architecture and training parameters were suitable for predicting the specific capacitance of ZnS nanoparticles.

3 Characterization

3.1 UV-Visible Absorption Spectroscopy

A double-beam SPECORD 200+ spectrophotometer purchased from Analytik Jena, Germany having a wavelength range of 190-1100 nm and is equipped with a deuterium and halogen lamp. 1 mg of material was dissolved in 15 mL of water, and the mixture was sonicated for 20 minutes at 40°C. 1 mL of solution was diluted to 10 mL with distilled water, and the solution was again sonicated for 10 minutes at 40 °C. The analysis was carried out in a quartz cuvette with a 10 mm path length.

3.2 Dynamic Light Scattering

Zeta-Sizer Nano (model ZSP Malvern Analytical Technology, UK) and Malvern zeta-sizer software (v 8.02) were used to analyze ZnS, CoS, and their mixed metal sulfides at various optimization levels for hydrodynamic size, polydispersity index, and zeta potential studies. A polystyrene cuvette was used to measure the size and polydispersity of the sample. For zeta potential investigation, a disposable folded capillary cell (DTS1070) was used. The temperature was fixed at 25°C. 173^{O} non-invasive backscatter mode was employed to determine the size and M3-PALS technique was used to evaluate the zeta potential.

3.3 X-ray Diffraction

Bruker D8 Advance X-ray diffractometer was used to record the sample's XRD diffraction peaks, using (Cu) Kα radiation at a wavelength of λ = 1.5406 Aº with a step size of 0.013°. The

View Article Online
DOI: 10.1039/D5MA00846H

generator was set at 40 mA and 45 kV, the scan range was 2θ = 20°-90°. X'PERT 3 software was employed to compare the results with reference peaks.

3.4 FT-IR Spectroscopy

A Perkin-Elmer device with Spectrum IR software version 10.62 was used to perform Fourier transform infrared spectroscopy (FTIR) studies of metal sulfide nanoparticles. The solid nanoparticles were reduced to powder and deposited to the ATR crystal. The attenuated total reflectance (ATR) mode was used to generate FT-IR spectra in the wavenumber range of 500 cm^{-1} to 4000 cm^{-1}.

3.5 Scanning Electron Microscopy

With an acceleration voltage of 1KV to 30KV, a high-performance SEM-3100 with a magnification of 300000× was used to study the surface morphology of the synthesized materials.

3.6 BET Analysis

Nitrogen adsorption-desorption measurements were carried out using a Quantachrome Nova Station B instrument. Approximately 95 mg of the sample was degassed at 150 °C for 10 hours to remove surface moisture and contaminants. The analysis was conducted at 77.3 K using nitrogen gas, with an equilibration time of 50/75 seconds (adsorption/desorption).

4 Results and Discussion

4.1 DLS-Based Optimization of Nanoparticles

4.1.1 Effect of Precursor Concentration

ZnS, CoS, and their mixed sulfide (ZnS:CoS 75:25, 50:50, and 25:75 ratio) nanoparticles were synthesized and characterized by UV-Vis spectroscopy, DLS, and zeta stability measurements. The UV-Visible analysis was performed in the range of 200 - 800 nm for all (mixed) metal sulfide nanoparticles and graphs are normalized at 216 nm as shown in Fig. 1a. The absorbance peaks of ZnS and CoS appear at 221 nm and 214 nm respectively which correspond to the literature values and confirm the formation of ZnS and CoS NPs [47, 48]. In the case of mixed metal sulfide (50:50) characteristics peaks of both ZnS and CoS are visible at 221 nm and 214 nm respectively which proves the synthesis of mixed metal sulfide nanoparticles. Fig. 1b describes the zeta potential of mixed ZnS-CoS nanoparticles prepared with different concentrations of salts. It is clear that the stability of mixed metal sulfides is less than that of pure metal sulfides except for 50:50, which is near to the stability of pure ZnS. Among all, pure cobalt sulfide nanoparticles are most stable followed by pure ZnS. The zeta potential values

can be influenced by many factors e.g. pH, ionic strength, the concentration of different components, and specific conditions used [48]. The hydrodynamic backscattered particle size of different ratios of metal sulfides is shown in Fig. 1c, where the hydrodynamic backscattered size of pure ZnS and CoS was found to be 406 nm and 245 nm respectively. It is clear that hydrodynamic backscattered size gradually decreases with the increase in the concentration of cobalt sulfide. The same trend was observed for the forward scattering angle except for cobalt sulfide which shows 707 nm size as shown in Fig. 1d. Fig. 1e expresses the PDI values that have no regular trend, however with the increasing concentration of cobalt in mixed sulfides result in lower PDI, hence better control in size.

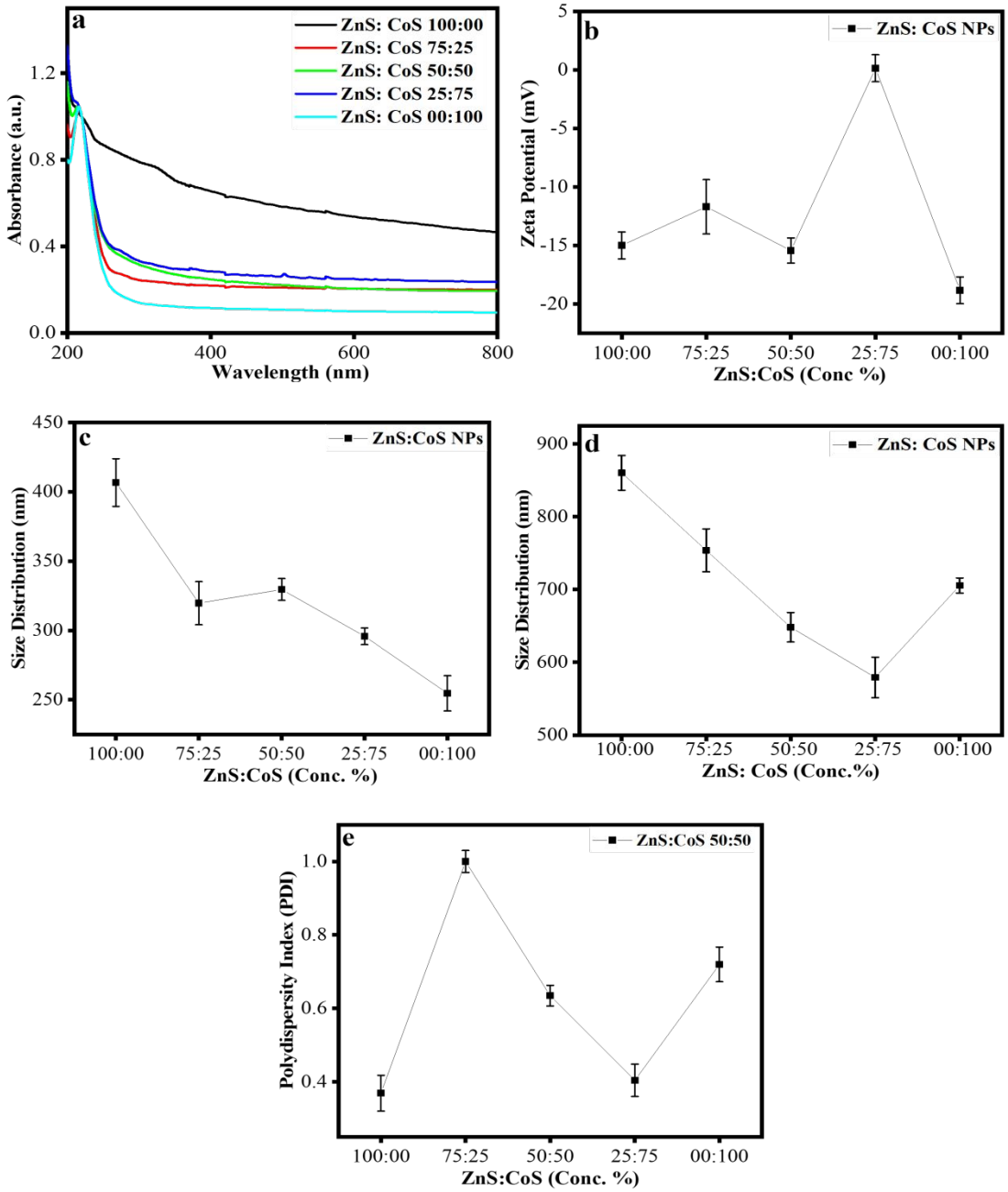

View Article Online
DOI: 10.1039/D5MA00846H

Figure 1: Characterization of mixed ZnS–CoS nanoparticles prepared at different concentration ratios: (a) UV–Vis absorption spectra, (b) zeta potential, (c) hydrodynamic size (backscattered), (d) hydrodynamic size (forward scattered), and (e) polydispersity index (PDI).

4.1.2 Effect of Temperature

The mixed sulfide (50:50) were chosen based on higher stability and were synthesized at 20℃, 40℃, 60℃, and 80℃. Fig. S3a shows the UV-Vis spectra of mixed ZnS and CoS nanoparticles prepared at these different temperatures. The graphs are normalized at 212 nm. The characteristic peaks as observed previously are also observed here, however no significant difference is observed in the UV-Vis peaks. Fig. S3b represents the zeta potential values of nanoparticles synthesized at these temperatures. It is clear that with the increase in temperature, there is a substantial decrease (negatively) in the zeta potential values, representing higher stability, hence mixed nanoparticles are more stable when synthesized at 80℃. Fig. S3c and S3d depict the backscatter and forward scatter hydrodynamic size distribution of the mixed ZnS-CoS nanoparticles synthesized at these temperatures. It is observed that backscattered size distribution decreases with the enhancement in the temperature that corresponds with the literature [29] as the reaction is relatively slow at lower temperatures causing the particles to grow and agglomerate, whereas faster kinetics play important role at higher temperatures causing smaller and uniform size of nanoparticles [49]. Since backscattering is sensitive to smaller particles while larger particles prefer to be scattered in a forward direction [29], therefore as a result when size is measured at the forward angle, it is always larger and generally a reversed sequence is observed as compared to size measured at the backscatter angle. As a result, forward scattering shows an increase in size with an increase in temperature. Overall, better control of size is observed at 80℃. The polydispersity index of mixed ZnS-CoS nanoparticles at these temperatures is shown in Fig. S3e where it is clearly observed that polydispersity continuously decreases as temperature rises, with the lowest polydispersity observed at 60℃, and after that, there is a slight increase in polydispersity at 80℃. Hence, with the rise in synthesis temperature of mixed metal sulfide nanoparticles, there is a shift from broad size distribution to uniform size distribution, and the best uniform size distribution is observed at 60℃.

4.1.3 Effect of pH

We chose 80℃ as an optimal temperature based on the higher stability and uniform small size of nanoparticles. The effect of pH was studied, where different pH were maintained i.e 3, 5, 7, 9, 11, 12, and 13. UV-Vis graphs of resulting nanoparticles are observed as shown in Fig. S4a

View Article Online
DOI: 10.1039/D5MA00846H

and are normalized at wavelength of 212 nm. Fig. S4b shows the zeta potential values of these mixed ZnS-CoS nanoparticles synthesized at different pH. Although there is no regular trend of zeta potential values, however better stability can be observed at higher pH values i.e., at pH = 11 and 13, as zeta potential decreases.

The backscatter hydrodynamic size of mixed metal sulfides prepared at different pH is shown in the Fig. S4c. Hydrodynamic radius (R_{hyd}) decreases first at pH 5, then steady increase in size with increase in pH is observed till pH 11, after which again there is decreasing trend in size. The hydrodynamic size at pH 13 is observed to be 262 nm. So a general trend could be explained as higher pH causes more stability and relatively smaller size, hence potential agglomeration is prevented at higher pH. Fig. S4d shows the forward scatter hydrodynamic size of the mixed sulfide nanoparticles. There is no regular trend of forward scatter hydrodynamic size, however with the variation of pH, minimum size is observed at pH 5. Fig. S4e depicts the polydispersity index of mixed sulfide nanoparticles synthesized at different pH, where we do not find regular trend of polydispersity index with the variation in the pH values. The highest polydispersity index (0.93) is observed at acidic pH 3, while the lowest PdI value (0.33) is observed at neutral pH. It means that at neutral pH, uniform size distribution of particles occur.

4.1.4 Effect of Addition of Sulfide Source

ZnS-CoS were synthesized at different times of addition of sulfide source (Na_2S), after the reaction started i.e., quick addition, 5-minute addition, 10-minute addition, and 20 minutes addition. Ideal pH 7 and temperature at 80℃ were maintained for 50:50 ratio of ZnS:CoS. UV-Visible spectra as shown in Fig. S5a shows no significant difference. Fig. S5b shows the zeta potential of synthesized mixed ZnS-CoS nanoparticles prepared by different times of addition of sulfide source. We can see that 5 minute addition has more negative values (-15.77 mV) with higher repulsion between the charged particles that prevents them from agglomeration [50], hence higher stability. Fig. S5c shows the hydrodynamic backscattered size of mixed ZnS-CoS nanoparticles synthesized at different times of addition of sulfide source. The back scattered hydrodynamic size increased with the increase in the time of addition till 10 minutes then a decrease in R_{hyd} was observed at 20 minutes of addition. The best control of size is depicted for quick addition followed by 5 minute addition. Fig. S5d shows the forward scattered hydrodynamic size. An increase in R_{hyd} is observed for 5 minutes then decrease for 10 minutes, and again increase for 20 minutes of addition. Fig. S5e shows that the polydispersity index of mixed metal sulfide nanoparticles synthesized at different times of addition of sulfide source are lowest at quick and

View Article Online
DOI: 10.1039/D5MA00846H

20 minutes addition, and highest at 5 and 10 minutes addition. Overall, size and PdI analyses show that the best reaction kinetics occur at quick addition, yielding the lowest size and PdI value.

4.1.5 Effect of PVA Ratios

Mixed ZnS-CoS nanoparticles were also optimized for different concentrations of PVA i.e.,m 0%, 0.5%, 1%, and 2%, after maintaining the ideal conditions i.e 50:50 ratio, pH 7, 80℃, and quick addition of sodium sulfide solution. UV-Visible spectra are shown in Fig. S6a.

Fig. S6b depicts the zeta potential of mixed metal sulfides synthesized with different concentrations of PVA. A steady decrease (negatively) in zeta potential is observed with the increase in the concentration of stabilizer. At 2% PVA concentration, zeta potential is more negative i.e. -17 mV. Hence decreasing zeta potential values with increasing stabilizer concentration indicates that stability increases by increasing stabilizer concentration. This is because stabilizers cap the nanoparticle's surface and prevent it from agglomeration [51]. In this way, mixed sulfide nanoparticles are highly stabilized by the addition of a capping agent. Fig. S6c demonstrates the backscattered hydrodynamic size of mixed metal sulfides synthesized with different concentrations of PVA. Backscattered hydrodynamic size steadily decreases with the increase in the amount of the PVA. For a maximum 2% concentration of stabilizer, a minimum size of 214 nm is achieved. Adding higher concentration of stabilizer prevents nanoparticles from agglomeration and leads to a reduction in the size of nanoparticles **[52]**. Fig. S6d demonstrates the forward scattered hydrodynamic size of the mixed metal sulfides. It is obvious that R_{hyd} decreases with an increase in the concentration of PVA and with 2% PVA concentration, the size is only 185 nm. The polydispersity of mixed sulfide nanoparticles is shown in Fig. 6Se. The PDI of mixed sulfide nanoparticles synthesized without stabilizer is lowest at 0.22, whereas an increase in the percentage of stabilizers (PVA) leads to a rise in the PDI value, reaching a maximum of 0.53 at 2%.

As a result of these investigations, large scale synthesis was performed for 50:50 ratios, pH 7, 80℃, quick addition of sodium sulfide solution, and 2% concentration of PVA. The optimized nanoparticles were further characterized and utilized for electrochemical studies.

4.2 Characterizations

4.2.1 FTIR Analysis

Fig. 2a depicts the FTIR spectra of ZnS NPs. The bands positioned at around 2855 cm^{-1} are due to C–H stretching vibrations of PVA [52]. The peaks appearing at 796 and 508 cm^{-1} are associated to Zn–S vibrations and are characteristic of cubic ZnS [53]. The broader peak at 3366 cm^{-1} corresponds to the stretching frequency of -OH group of PVA [54]. The absorption

View Article Online
DOI: 10.1039/D5MA00846H

band at 1626 cm[1] is due to C–C stretching vibrations [55]. The peak appeared at 1135 cm[−1] is associated to C-C and C-O-C bond vibration [56]. Fig. 2b depicts the FTIR analysis of CoS. Peaks appearing at 3202 cm^{-1} and 1068 cm^{-1} correspond to O-H stretching and C-O stretching respectively [54]. The peak positioned at 1670 cm^{-1} represents the bending of water molecules adsorbed on the surface of cobalt sulfide [57]. Fig. 2c describes the FTIR analysis of optimized ZnS-CoS mixed metal sulfides. Peaks indicated at 1605 cm^{-1} is associated to water molecules. Peak appearing at 607 cm^{-1} is related to metal sulfide group [58].

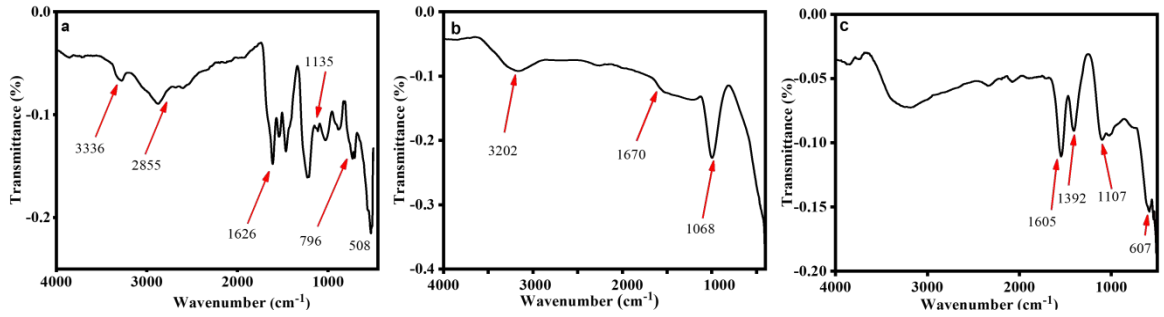

Figure 2: FTIR spectra of (a) ZnS nanoparticles, (b) CoS nanoparticles, and (c) optimized mixed ZnS–CoS nanoparticles, showing the characteristic vibrational bands corresponding to metal–sulfur stretching and surface functional groups.

4.2.2 XRD Analysis

Using a Cu anode as the radiation source, a Bruker D8 Advance diffractometer was used to study the crystalline structure of pure and mixed (50:50) metal sulfide nanoparticles by X-ray diffraction (XRD). The 2θ values in XRD spectra correspond to angles at which the crystal lattice deflects X-rays. Each peak indicates a distinct set of crystal planes. The compound's crystallinity and crystallite size can be determined by these peaks. The crystalline structure of ZnS NPs is determined by analyzing their diffraction pattern as shown in Fig. 3a which shows phase purity. Three significant peaks are observed at 2θ = 28.08^{O}, 47.66^{O}, and 56.85^{O} aligned to 111, 220, and 311 planes respectively. All the crystallite peaks have solid alignment with standard JCPDS card no # 01-080-0020 which verifies the blende cubic phase of ZnS nanoparticles [43]. Fig. 3b shows the XRD pattern of cobalt sulfide nanoparticles. Prominent peaks at 2θ = 29.91^{O}, 36.62^{O}, 47.32^{O}, and 52.29^{O} corresponding to 100, 101, 102, 110 lattice planes respectively are observed having strong agreement with the JCPDS card no # 65-3418 that validate hexagonal CoS [58]. Fig. 3c depicts the XRD pattern of ZnS-CoS, characteristics peak at 2θ = 56.85^{O} confirming the presence of ZnS in optimized ZnS-CoS mixed metal

View Article Online
DOI: 10.1039/D5MA00846H

sulfides. While peaks observed at 2θ = 29.91^{O}, 36.62^{O}, 47.32^{O}, and 52.29^{O} confirm the presence of CoS in mixed metal sulfides.

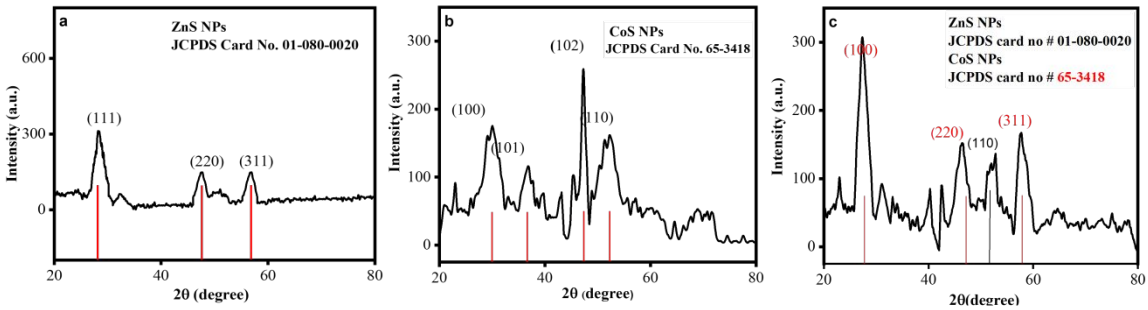

Figure 3: XRD patterns of (a) ZnS nanoparticles, (b) CoS nanoparticles, and (c) optimized mixed ZnS–CoS nanoparticles, confirming the crystalline phases and structural composition of the synthesized materials.

4.2.3 SEM Analysis

Zinc sulfide's morphological analysis is carried out using scanning electron microscopy. As seen in Fig. 4a the SEM picture of the synthesized zinc sulfide NPs is observed at 50000× magnification at a 200 nm scale bar that reveals its nano morphology. Cobalt sulfide's morphological analysis is illustrated in Fig. 4b with a rod-like morphology. Mixed ZnS-CoS (50:50) nanoparticles are shown in Fig. 4c with a particle-like morphology.

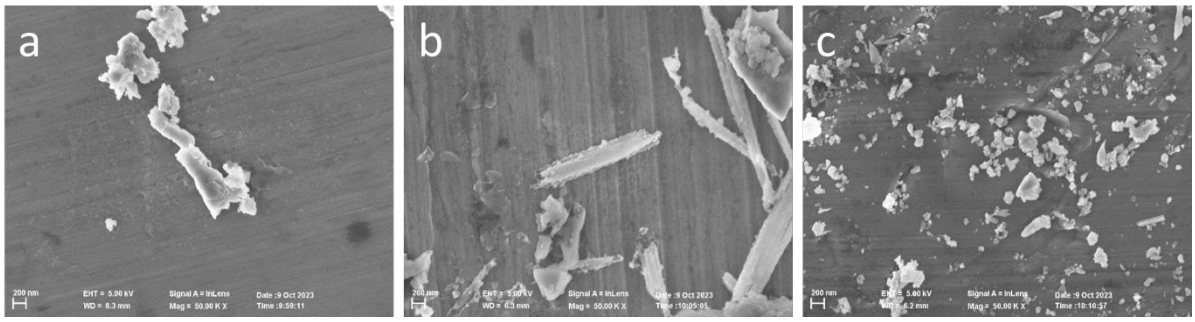

Figure 4: SEM micrographs of (a) ZnS nanoparticles, (b) CoS nanoparticles, and (c) optimized mixed ZnS–CoS nanoparticles, illustrating the surface morphology of the synthesized materials.

4.2.4 BET Analysis

Nitrogen adsorption-desorption analysis was conducted to evaluate the textural properties of the optimized ZnS-CoS (Fig. 5 a, b). The BET surface area, calculated using the multi-point

View Article Online
DOI: 10.1039/D5SA00846H

method, was found to be 386.5 m²/g, while Langmuir surface area was found to be 552.1 m²/g, which is higher than the BET due to its assumption of monolayer adsorption, confirming a high surface area that supports enhanced charge accumulation. The C constant value of 72.89 suggests a strong interaction between the nitrogen adsorbate and the surface, confirming the material's affinity for gas molecules. The total pore volume, as determined by the DFT model, was 0.197 cc/g, closely matching the micropore volumes obtained from the HK (0.1899 cc/g) and SF (0.1735 cc/g) models, indicating that a significant portion of porosity arises from micropores. The average pore radius, based on DFT, was 6.159 Å (equivalent to a diameter of 1.23 nm), which falls within the microporous range (<2 nm). In contrast, the BJH method showed a much lower cumulative surface area (10.96 -13.89 m²/g) and smaller pore volume (~0.028-0.029 cc/g), with a pore diameter centered around 4.66 nm (23.3 Å), revealing a minor mesoporous contribution.

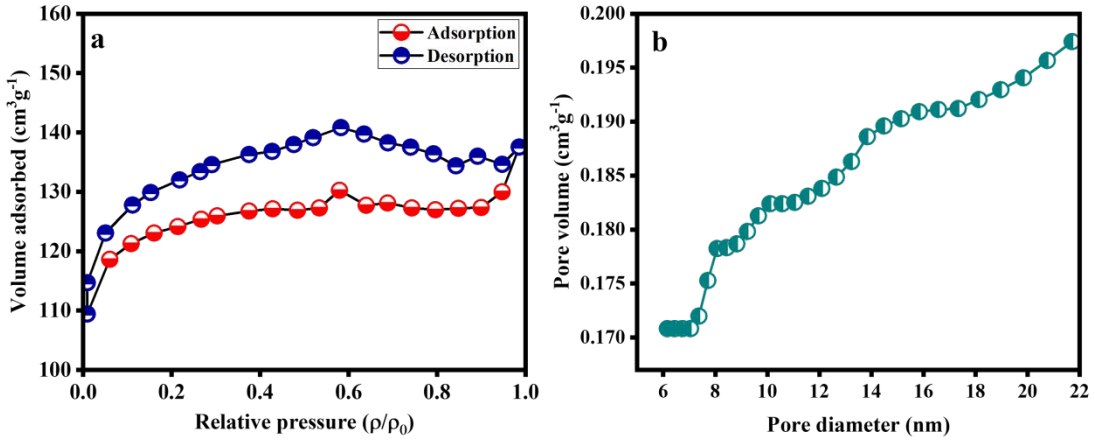

Figure 5: (a) N_2 adsorption–desorption isotherm and (b) pore size distribution curve (derived from BJH desorption data) of the optimized mixed ZnS–CoS nanoparticles, confirming their specific surface area and mesoporous structure.

4.3 Electrochemical Studies

To evaluate the charge storage capacity and the capacitive response of ZnS, CoS, and optimized ZnS-CoS; cyclic voltammetry (CV), galvanostatic charge-discharge (GCD), and impedance spectroscopy (EIS) were carried out in aqueous solution using 3 3-electrode system. Cyclic voltammetry results are shown in Fig. 6a, 6b, and 6c for ZnS, CoS, and ZnS-CoS nanoparticles respectively, which were obtained at a scan rate of 5 mVs^{-1} to 100 mVs^{-1} with a fixed potential window of -0.4 to 0.6V for all samples.

View Article Online
DOI: 10.1039/D5MA00846H

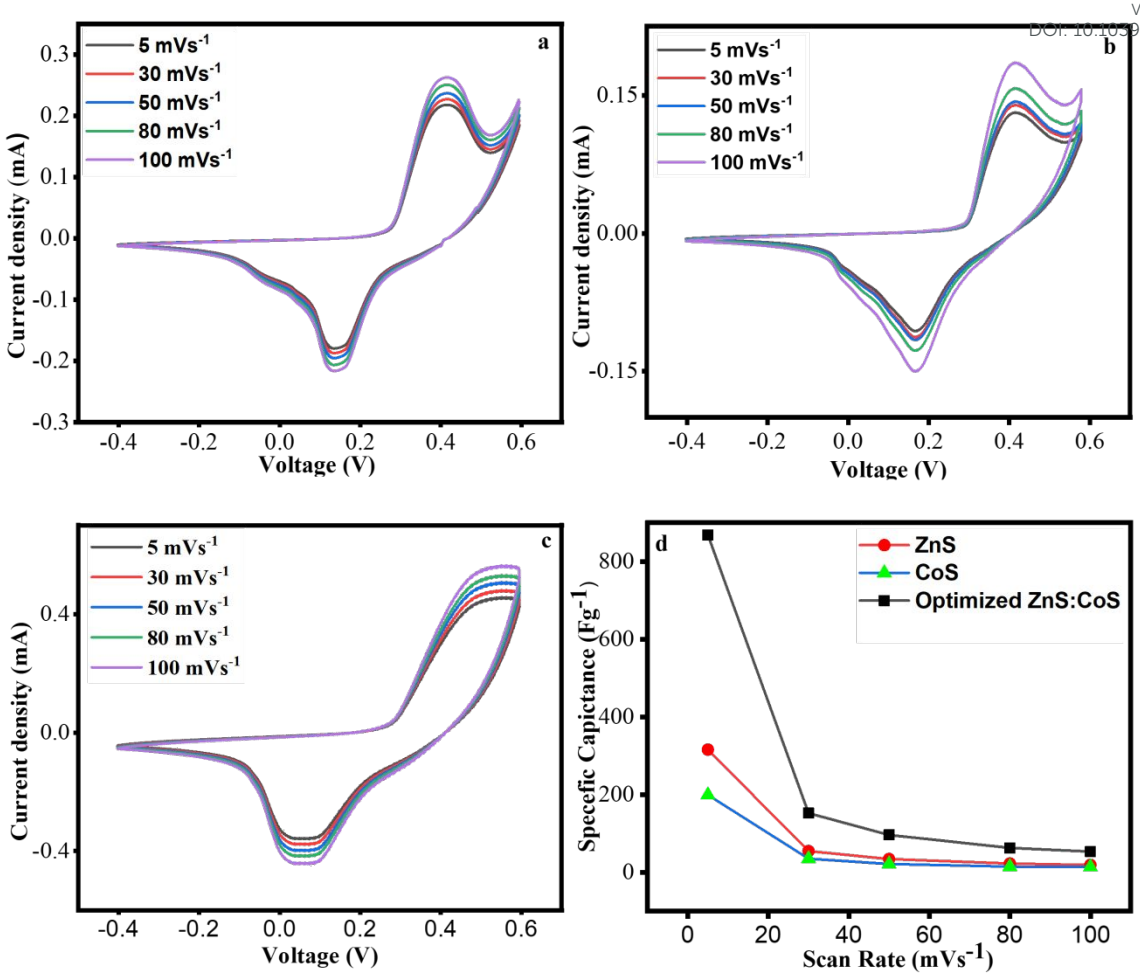

Figure 6: Cyclic voltammetry (CV) curves recorded at different scan rates within a fixed potential window for (a) ZnS nanoparticles, (b) CoS nanoparticles, and (c) optimized mixed ZnS–CoS nanoparticles. (d) Comparative plot of specific capacitance as a function of scan rate for all three electrodes, highlighting the superior electrochemical performance of the mixed ZnS–CoS system.

The specific capacitance is calculated by using equation 1 for ZnS, CoS, and optimized ZnS-CoS at different scan rates from 5 mVs^{-1} to 100 mVs^{-1} in the potential window of -0.4 to 0.6 V. Excellent results are obtained at 5 mVs^{-1} for each material. For ZnS it is 315 F/g and for CoS it is 199 F/g. For mixed metal sulfides, which were optimized at various conditions, depict extraordinary results as observed in Fig. 6d. Specific capacitance was obtained to be 868 F/g for optimized mixed metal sulfides which is more than four times of CoS and nearly 3 times of ZnS. With an increase in the scan rate, there is an exponential decrease in the specific capacitance due to limited time availability among the electrode and electrolyte intercalation [59].

The CV curve maintained at a higher scan revealed excellent stability of the electrode materials. In all samples, peak current increases with the increase in the scan rate that is associated with the redox reaction. In Fig. 6c the large integration area of optimized ZnS-CoS is attributed to the synergetic effect of ZnS and CoS in mixed metal sulfides. From cyclic voltammetry results, following conclusion can be drawn

1- The voltammogram's peaks seem to be well-defined despite some broadening, particularly at higher scan rates. This broadening may indicate quasi-reversibility since it implies a deviation from perfect reversibility.

2- At higher scan rates (100 mV/s), the anodic and cathodic peak separation appears to be greater than the ideal 59 mV predicted for a fully reversible process. A quasi-reversible process is characterized by an increasing ΔEp with scan rate.

3- Peak separation rises with increasing scan rate (from 5 mV/s to 100 mV/s), which is characteristic of quasi-reversible reactions. The peak separation is constant for reversible processes regardless of scan rate.

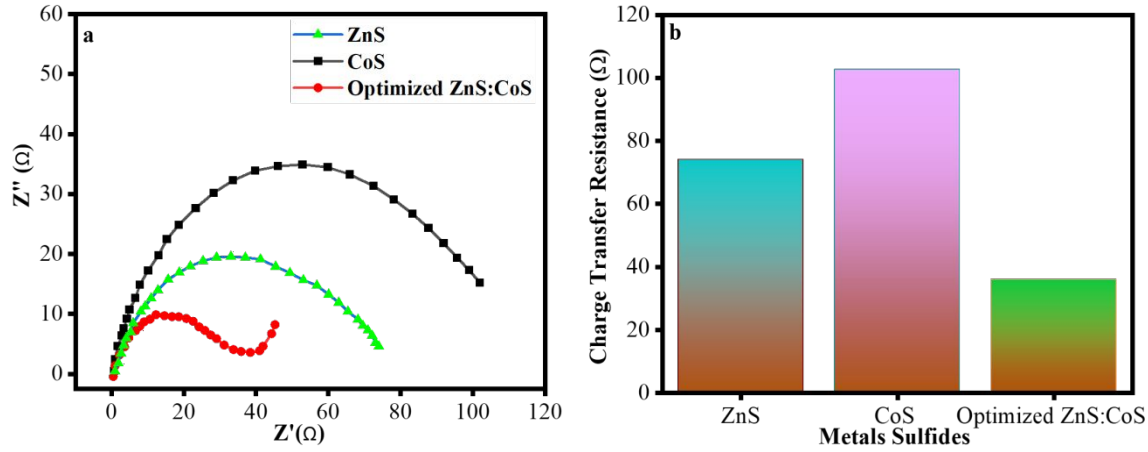

Figure 7: (a) Nyquist plots of ZnS, CoS, and mixed ZnS–CoS electrodes, illustrating their electrochemical impedance behavior. (b) Comparative analysis of charge-transfer resistance (R_{ct}) values, demonstrating the enhanced conductivity and lower resistance of the mixed ZnS–CoS electrode.

EIS was applied to achieve the kinetics of the charge transfer. Common impedance plots comprise of three primary regions. A high-frequency region is represented by a semicircle whose diameter denotes the charge-transfer resistance R_{ct}, a low-frequency region, and the intercept at the real axis indicates the resistance of the solution. At similar conditions, we performed electrochemical impedance spectroscopy for ZnS, CoS, and optimized ZnS-CoS,

View Article Online
DOI: 10.1039/D5MA00846H

and resulting impedance plots are illustrated in Fig. 7a. Fig. 7b shows that optimized ZnS-CoS demonstrates the lowest R_{ct} (35.88) among these three materials, also shown in **table 1**. The rapid movement of charge carriers in an electrochemical process are attributed to the synergistic effect of ZnS and CoS, which provide superior conductive support. It suggests that the maximum number of charged ions reach the surface of the electrode to support the electrochemical redox process. Therefore impedance study verifies that the optimized ZnS-CoS is an outstanding material with excellent specific capacitance and superior rate performance [60].

Table 1: Charge Transfer resistance of pure and mixed metal sulfides.

Metal Sulfides	**Charge Transfer Resistance (R_{ct}) (Ω)**
ZnS	74.20
CoS	102.06
ZnS-CoS	35.88

To assess the charge storage capacity of ZnS, CoS, and ZnS-CoS, Galvanostatic charge-discharge study was carried out at different current densities of 2, 4, 5, and 6 A/g at fixed potential -0.4 to 0.6, as depicted in Fig. 8a, 8b and 8c. GCD curves depicts nonlinear behavior that demonstrate the Faradic reactions between the electrode materials and electrolyte solution that has the strong agreement with CV results. Specific capacitance calculated from GCD profile at various current densities is slightly higher than the specific capacitance calculated from CV. Decrease in the specific capacitance with increasing current densities is observed due to fact that electrolyte ions do not have enough time to migrate into pores of materials [61]. It is clear from **Table 2** that DLS optimized ZnS-CoS depicts an extraordinary specific capacitance of 1156 F/g at 2 A/g, which is four times higher than that of ZnS and CoS, due to the synergetic effect of Zn and Co.

The specific capacitance of cobalt sulfide drops drastically from 130 Fg^{-1} at 5 A g^{-1} to 7.44 Fg^{-1} at 6 Ag^{-1} (Table 2). This rapid drop is explained by slow charge-transfer kinetics and limited ion diffusion at high current densities, which significantly reduce the effective contact time between electrolyte ions and the active electrode surface [62]. Cobalt sulfide depicts a pronounced decrease in specific capacitance as the current density increases and it is well documented in the literature. For instance, Sathiskumar et al. reported a specific capacitance of 348 Fg^{-1} at 1 A g^{-1}. At higher current densities, this capacitance dropped significantly to 100 Fg^{-1} at 20 A g^{-1}, or a 71% reduction. [63]. By contrast, composites often retain specific

View Article Online
DOI: 10.1039/D5MA00846H

capictance even at high current density [64]. Additionally, our EIS results are also consistent with the specific capacitance values listed in Table 2. The significant loss in capacitance at higher current densities can be explained by the comparatively high charge-transfer resistance of cobalt sulfide (102.66 Ω). Higher surface charge resistance indicates the sluggish charge transfer kinetics that result in poor electrochemical performance [65].

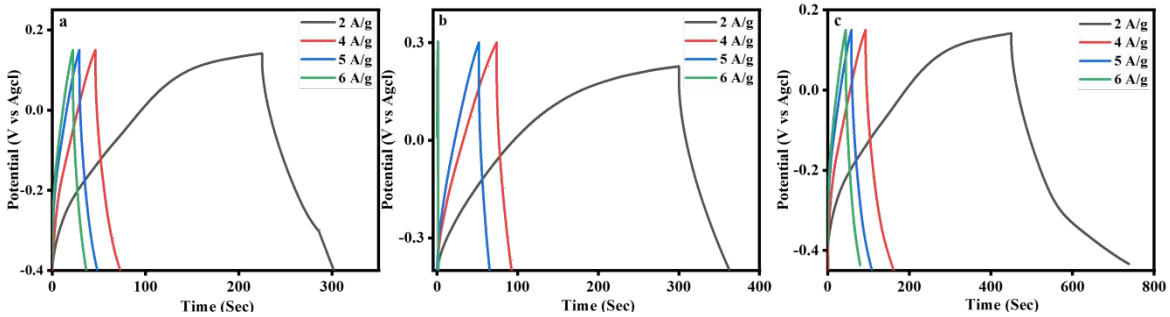

Figure 8: Galvanostatic charge–discharge (GCD) profiles of (a) ZnS, (b) CoS, and (c) optimized ZnS–CoS electrodes recorded at various current densities, demonstrating their charge storage behavior and capacitance characteristics.

Table 2: Specific capacitance values against various current densities for ZnS, CoS, and optimized ZnS-CoS electrodes.

Current Densities (A/g)	**2**	**4**	**5**	**6**
ZnS	264	208	190	168
CoS	248	152	130	7.44
ZnS-CoS	1156	568	540	432

Table 3: Specific capacitance, energy density, and power density at different current densities for optimized ZnS-CoS electrodes

Current Density (A/g)	**2**	**4**	**5**	**6**
Specific capacitance (F/g)	1156	568	540	432
Energy density (Wh/Kg)	194	95	90	72
Power density (W/Kg)	2420	4840	6050	7260

Energy density and power density are also calculated by using equations *3* and *4* provided in the experimental section. As shown in **Table 3,** DLS optimized ZnS-CoS exhibits excellent power density of 7260 (W/Kg) at the energy density of 72 (Wh/Kg) at 6 A/g, which is decreased to 2420 (W/Kg) at the energy density of 194 (Wh/Kg) at 2 A/g, indicating higher rate capability

View Article Online
DOI: 10.1039/D5MA00846H

at higher current density. The relation between power density and energy density is illustrated in the Ragone plot Fig. 9a Cyclic stability is the key parameter to decide the durability and efficiency of materials. Cyclic stability of optimized ZnS-CoS was determined by performing repeated charge-discharge tests at a very high current density of 20 Ag^{-1} over 10000 cycles, as expressed in Fig. 9b 93.87% capacitance is retained over 10000 cycles. Moreover, from start to end no structural collapse; and stability were observed resulting in high conductivity of DLS optimized ZnS-CoS mixed metal sulfides. This can be confirmed by the GCD curves of first and last ten cycles, as shown in Fig. 9c and 9d respectively.

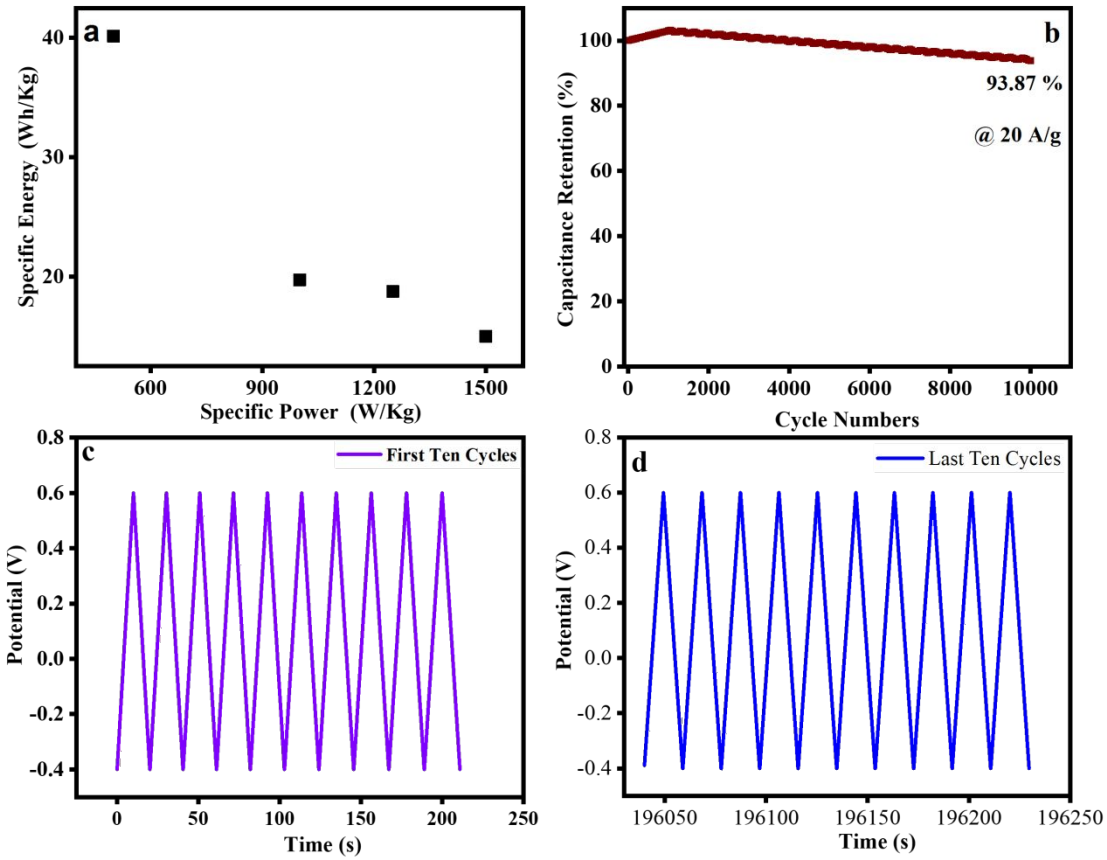

Figure 9: (a) Ragone plot showing the relationship between energy density and power density for the optimized ZnS–CoS electrode. (b) Cycling stability performance of the optimized ZnS–CoS electrode over 10,000 charge–discharge cycles, confirming its long-term electrochemical durability c) GCD curves of the first ten cycles d) GCD curves for the last ten cycles.

To support the experimental part in qualitative manner, mathematical Dunn's model was applied. CV curves were further investigated to explore the charge storage mechanism. For this

View Article Online
DOI: 10.1039/D5MA00846H

purpose, power law equation is used to describe the relationship between the specific current and scan rate applied. The results are presented in Fig. 10.

$$i = av^b \qquad 5$$

$$log(i) = log\ a + b\ log\ v \qquad 6$$

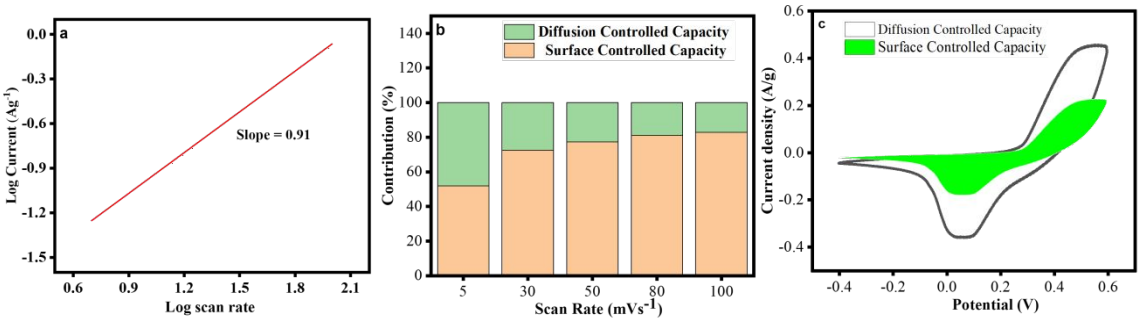

Figure 10: (a) Linear relationship of log(i□) versus log(v) for the optimized ZnS–CoS electrode, (b) bar chart showing the relative capacitance contribution at different scan rates, and (c) CV curves analyzed using Dunn's method to distinguish the diffusive and surface-controlled capacitance contributions.

In equations *5* and *6*, i, a, and b represent current, scan rate, and constants, respectively. With the help of this equation, we can calculate the factor b for which values range from 0.5 to 1. The charge storage mechanism is completely surface controlled when the value of b is close to 1. A value of b approaching 0.5 indicates a totally diffusion-controlled process. Plotting the log of a specific current against the log of scan rate in equation *6* provides the value of factor b that is calculated from the slope of the straight line. As depicted in Fig. 10a the value of b is 0.91 that is close to 1 describing that the mechanism is surface controlled. The equation *7* shows how to calculate the percentage contribution.

$$i(v) = k_1 v + k_2 v^{1/2} \qquad 7$$

Here, k_1 and k_2 indicate the constant, while k_1v and $k_2v^{1/2}$ are used to describe surface-controlled capacity and diffusion-controlled capacity, respectively. Fig. 10b represents the surface-controlled capacity of optimized ZnS-CoS which was found to be 52.30% at 5 mV. It is clear in Fig. 10b that the diffusion-controlled contribution decreases at higher scan rates because the electrolyte ions do not have enough time to absorb onto the electrode material. CV curves expressing the diffusive and surface-controlled capacitance contribution of ZnS-CoS NPs by Dunn's method is shown in Fig. 10c.

View Article Online
DOI: 10.1039/D5MA00846H

In **Table 4**, a comparative analysis of specific capacitance, energy density, power density, and cyclic stability are shown for similar materials, as compared to our optimized ZnS-CoS mixed metal sulfide electrodes, which show a significant enhancement of energy density and power density values for our optimized material.

Table 4: Comparative analysis of optimized ZnS-CoS mixed metal sulfide electrodes with other literature reported values.

Materials	Specific capacitance (F/g)	Energy density (Wh/kg)	Power density (W/kg)	Cyclic stability (%)	Ref.
Zn-Co-S	1269.1	45.4	805.0	91.6%	[20]
Multilayer dodecahedrons Zn-Co sulfide	971.01	31.63	8.09	90.3%	[66]
WS2@NiCoS	784.38	49.47	1212.30	93.23 %	[67]
Z ZCS/GO/CN	811	33.3	624	81.08 %	[68]
Co-Mn-S	537	73.52	10,200	90.03%	[69]
Zn-C0-S nanostrip	830	19.0	514	76 %	[70]
Co-Zn- C-S	815	-	-	83.9 %	[71]
Zn-Co Bimetal Sulfides	6.22 Fcm^{-2}	0.124mWh	21$mWcm^{-2}$	68.4 %	[68]
Nanostructured CoS	1056	31.4	200	90 %	[70]
ZnS nanowires	781	51	200	87 %	[71]
rGO/ZnCoS	891	29	2215	99 %	[68]
DLS Optimized ZnS-CoS	1156	194	7260	93.87 %	**Our Work**

Zinc and cobalt mixed metal sulfides have porous structures that give large gaps and open channels which increase ion diffusion and charge transport and act as promising materials for supercapacitors [72]. Hydroxide ion from KOH interacts with mixed metal sulfides that promotes reversible Faradic reaction [73]. The synergistic effect of zinc, cobalt, and sulfur increases the electrical conductivity which leads to a fast and reversible charge-discharge cycle [20]. The synergistic effect also provides an enhanced surface area [74] resulting in better charge storage. All these features make our optimized mixed metal sulfides promising materials for supercapacitor applications. The proposed mechanism for charge transfer at electrodes is shown in Scheme 1.

View Article Online
DOI: 10.1039/D5MA00846H

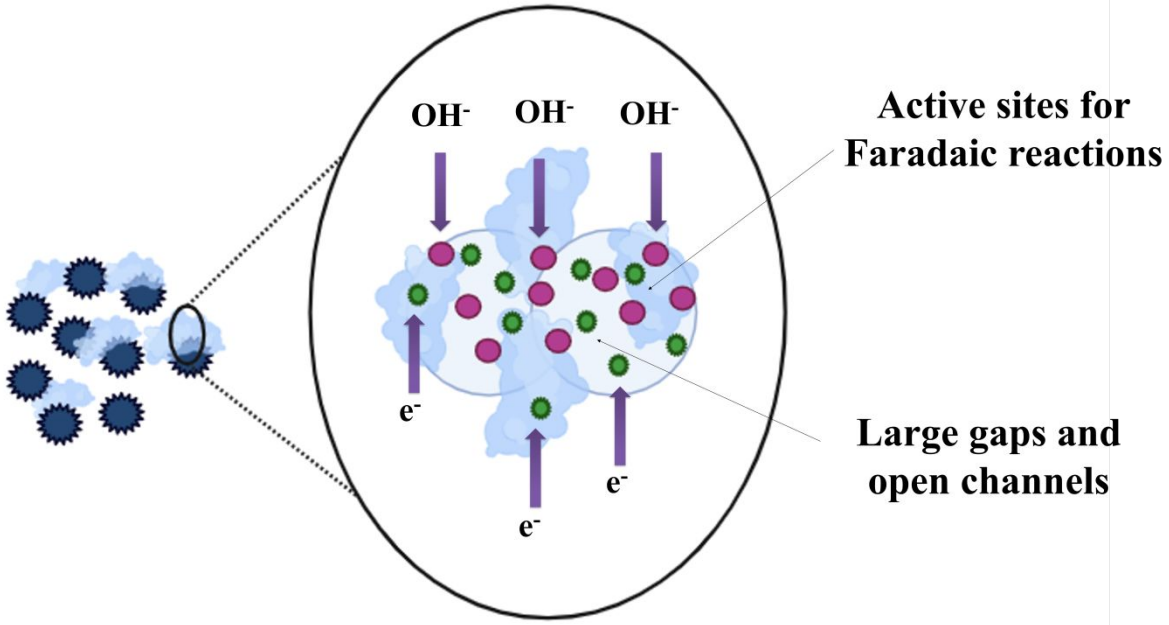

Scheme 1.: The proposed schematic shows the mechanism involved in the charge storage performance between optimized ZnS-CoS leading to excellent electrochemical properties and its interaction with the electrolyte during electrochemical process.

4.4 DFT studies

We also computationally calculated the band gaps of CoS, ZnS, and ZnS-CoS using GAUSSIAN 09 software with a PM6 basis set (a semi-empirical method). It is a reliable method for accurately predicting electronic properties. The calculated band gaps for ZnS, CoS, and the ZnS-CoS mixed sulfide are 2.51 eV, 2.75 eV, and 2.53 eV respectively (**table 5**). Computationally obtained HOMO-LUMO orbitals of ZnS, CoS, ZnS-CoS NPs are shown in Fig. 11. The results indicate that by forming a structure of ZnS-CoS, the band gap is the lower side, indicating an enhancement in electronic conductivity for mixed sulfides.

Table 5: HOMO and LUMO energies and bandgap in eV for ZnS, CoS, and ZnS-CoS NPs.

Material	E_{HOMO} (eV)	E_{LUMO} (eV)	$E_{L\text{-}H}$ gap (eV)
ZnS	-6.72039	-4.20143	2.51896
CoS	-11.6110	-8.85866	2.75234
ZnS-CoS	-10.8105	-8.28042	2.53008

View Article Online
DOI: 10.1039/D5MA00846H

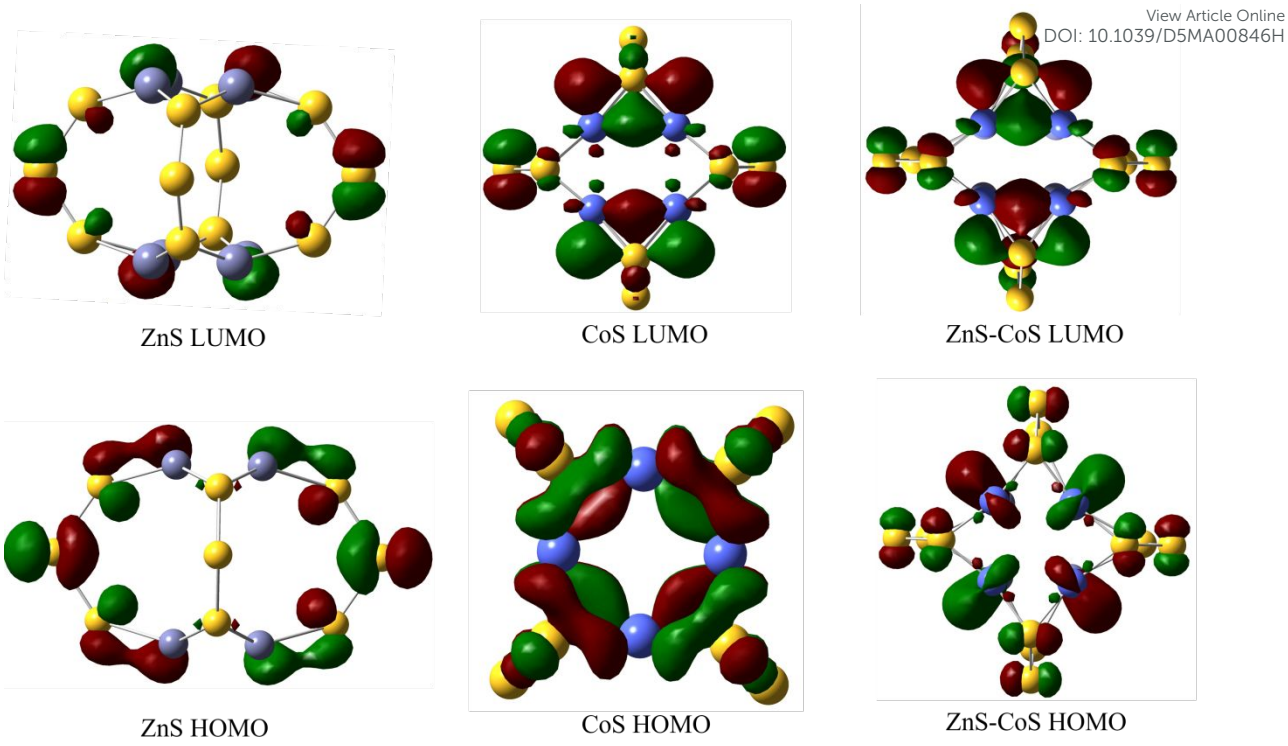

Figure 11: Computationally derived HOMO–LUMO orbital distributions of ZnS, CoS, and ZnS–CoS nanoparticles, illustrating the electronic structure and frontier molecular orbitals responsible for their charge transfer behavior.

The reduced band gap suggests better electron mobility for the ZnS-CoS and correlates with the improved electrochemical performance and enhanced charge storage capability as observed in the experimental results. Specifically, the cyclic voltammetry (CV) analysis revealed that the specific capacitance values were 264 F/g for ZnS, 248 F/g for CoS, and significantly higher 1156 F/g for the ZnS-CoS mixed sulfide, measured at a scan rate of 2 mV/s. The results also complement electrochemical impedance spectroscopy (EIS) analysis which demonstrated a lower charge transfer resistance for the ZnS-CoS mixed sulfide, confirming its superior electrical conductivity.

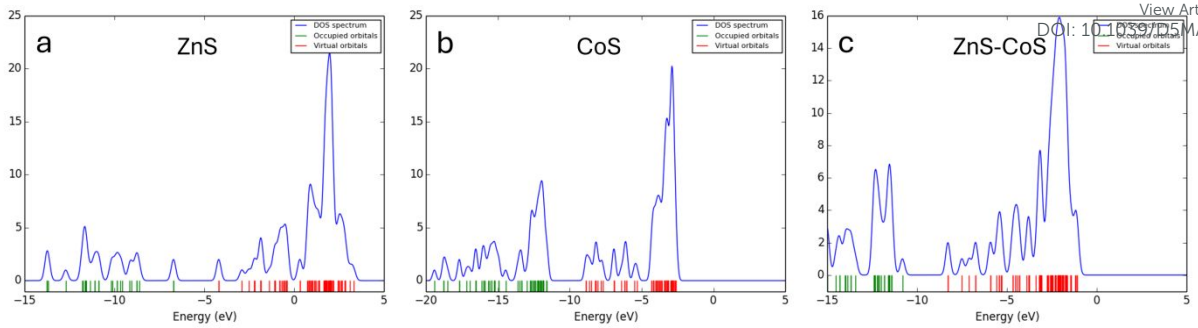

Figure 12: Density of states (DOS) spectra of ZnS, CoS, and ZnS–CoS nanoparticles, highlighting the electronic states near the Fermi level and their role in governing charge transport properties.

The density of states (DOS) analysis is shown in Fig. 12a, 12b, and 12c indicating that electron transfer between the valence and conduction bands is crucial for determining their conductivity. The Fermi level lies between these two bands, affecting the overall electron transfer mechanism. The DOS analysis provides insights into energy level formation, particularly the lowest unoccupied molecular orbital (LUMO) values. For example, in Fig. 12 the LUMO of ZnS is observed at -4.20 eV and for CoS, it is observed at -8.85 eV. When mixed sulfides are formed i.e., ZnS-CoS, the LUMO value is observed at -8.28 eV. These findings, also supported by computational and electrochemical analyses, illustrate that the synergistic effects are observed after mixing, on the electronic structure and capacitive performance. Hence, ZnS-CoS achieves better electrochemical performance due to its improved conductivity, as predicted by computational calculations.

4.5 Machine learning models' performance

This study utilized RSM, TPOT, ANN, and stacking regressor models to accurately verify the experimental specific capacitance of ZnS. In the present study, potential window, current density, and scan rate were input features, while specific capacitance was the output feature. Performance was evaluated on the basis of R^2 and RMSE metrics. Models were performed at different scan rates (5, 30, 60, 80, 100) mV/s. For stacking regressor at different scan rates (5, 30, 60, 80, 100) mV/s, MSE values of 0.002236, 0.002349,0.002487, 0.002761, 0.003014 were obtained respectively with corresponding R^2 values of 0.672140, 0.682545, 0.691387, 0.693611, 0.695586 as shown in Fig. 13. It is clear from the figure that there is a slight increase in R^2 values with an increase in the scan rate, which indicates that the model performs outstandingly at higher scan rates and the best results were obtained at 100 mV/s. It might be due to the reason that at a faster scan rate, models can process data points faster, leading to

View Article Online
DOI: 10.1039/D5MA00846H

enhanced overall prediction time. RSM performed the worst, with an R^2 of 0.46, RMSE of 0.42, and MAE of 0.33 (Fig. S7). TPOT improved the fit, resulting in R^2 of 0.57 with RMSE of 0.36 and MAE = 0.28 (Fig. S8). ANN showed slight improvement with R^2 = 0.57, RMSE = 0.34, and MAE = 0.26 (Fig. S9), indicating its ability to handle nonlinear datasets. The Stacking Regressor had the highest predictive accuracy, with R^2 = 0.67, RMSE = 0.28, and MAE = 0.21 (Fig. 13). Overall, the ranking of model performance was stacked regression > ANN > TPOT > RSM. These findings clearly show that the ensemble approach is the most reliable method for modeling the nonlinear capacitance behavior of the electrode system.

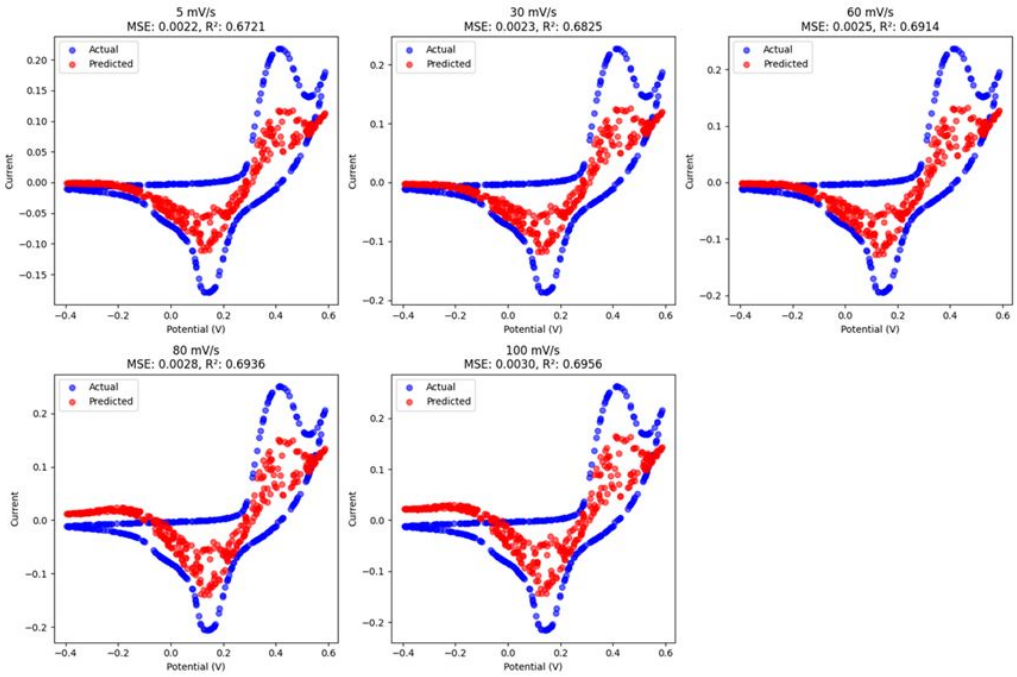

Figure 13: Comparison between experimental results and stacking regressor model predictions at different scan rates.

Furthermore, it is clear from the above discussion that the Artificial Neural Network (ANN) performed better in terms of prediction than the RSM regression model. The accuracy of the ANN model is attributed to its flexibility in capturing nonlinear behavior [75, 76]. It is well documented in literature. For instance, Khoshraftar et al. used both RSM and an ANN to model CO_2 adsorption on Fe–Ni/AC-modified carbon nanotubes. The ANN model achieved R^2=0.9990 (MSE=4.247×10^{-4}), whereas the RSM model had Predicted R^2=0.8899 [77]. In another study Luan et al. optimized a PVB synthesis using both RSM and ANN. Their results show RSM: R^2=0.9865, RMSE=0.4754; versus ANN: R^2=0.9962, RMSE=0.2551 [78]. In short, ANN models frequently achieve superior predictive accuracy and robustness than RSM because they can fit the interacting nonlinear behavior more flexibly.

View Article Online
DOI: 10.1039/D5MA00846H

Although extensive work has been reported on mixed transition metal sulfide nanoparticles, very limited attention has been given to controlling their particle size and stability. Since parameters such as precursor concentration, pH, temperature, reagent addition rate, and stabilizer concentration [28,29] directly influence size, shape, and surface chemistry, their optimization is essential for tuning electrochemical performance. Previous studies suggest that particle size and morphology control [36] can significantly enhance the properties of TMS-based electrodes; however, systematic strategies for improving specific capacitance, power density, and energy density remain lacking. In this work, we addressed this gap by optimizing key synthesis parameters to achieve controlled nanoparticle characteristics. The improved size and morphology directly contributed to enhanced electrochemical performance, demonstrating the importance of controlled synthesis in advancing TMS-based energy storage materials. For instance, Muhammad Sufyan Javed et al. reported a specific capacitance of 110 F/g for ZnS@$FeSe_2$ nanostructures [79], A. Shah et al. achieved 95 F/g for ZnS/$CuSe_2$//AC [80], while Hongxia Wang et al. reported 200 F/g for $Cu_5Sn_2S_7$/ZnS [81]. These earlier studies did not involve optimization of nanoparticle characteristics. In contrast, our optimized nanoparticles achieved a much higher capacitance of 1156 F/g, along with improved power density and energy density (Table 4), demonstrating that careful optimization of synthesis parameters is a highly effective strategy for advancing the performance of TMS-based energy storage materials.

In addition, our study introduces novelty by predicting the specific capacitance of ZnS by using machine learning models for the first time, at different scan rates, which has not been reported before. Unlike conventional ML approaches that face issues like overfitting and poor interpretability, we applied linearized data with advanced ML to achieve more robust and reliable predictions. Furthermore, DFT calculations revealed a reduced band gap in Zn–CO–S, which directly correlates with enhanced electrochemical properties, thereby reinforcing the experimental outcomes

5 Conclusion

In this study, we successfully synthesized and optimized zinc cobalt sulfide (ZnS-CoS) nanoparticles using the co-precipitation method, followed by an in-depth optimization process utilizing Dynamic Light Scattering (DLS). The optimization was systematically carried out by varying crucial synthesis parameters, including temperature, pH, reagent addition rate, and stabilizer concentration, to achieve well-dispersed, stable nanoparticles with controlled size

View Article Online
DOI: 10.1039/D5MA00846H

and morphology. The influence of these parameters on hydrodynamic size, polydispersity index (PDI), zeta potential, and overall electrochemical properties was carefully analyzed. The optimized ZnS-CoS nanoparticles exhibited remarkable electrochemical performance, achieving an exceptional specific capacitance of 1156 F/g at 2 A/g, which is significantly higher than the individual ZnS and CoS electrodes. Furthermore, the energy density and power density were found to be 194 Wh/kg and 7260 W/kg, respectively, demonstrating a substantial enhancement over conventional transition metal sulfide-based electrodes. The electrochemical impedance spectroscopy (EIS) results confirmed a lower charge transfer resistance (35.88 Ω), which facilitated faster ion transport and improved electrical conductivity. Additionally, galvanostatic charge-discharge (GCD) analysis indicated excellent rate capability and high capacitance retention, with the optimized ZnS-CoS electrode maintaining 93.87% of its initial capacitance after 10,000 continuous charge-discharge cycles. This highlights its superior stability and durability, making it a highly promising material for long-term energy storage applications. To further understand the charge storage mechanism, Dunn's power law model was applied, revealing that the ZnS-CoS electrode exhibited a dominant surface-controlled capacitive contribution of 52.30% at a scan rate of 5 mV/s, further supporting its excellent charge storage capability. Computational calculations, including Density of States (DOS) and HOMO-LUMO energy gap analysis, confirmed the synergistic effect of Zn and Co, resulting in enhanced electronic conductivity and improved charge transport properties. Stacking regressor, TPOT, ANN, and RSM models were applied to verify the experimental specific capacitance of ZnS. The performance metrics of these models follow the ranking of stacked regression > ANN > TPOT > RSM. This study demonstrates how well the stacking regression model can be used to improve electrical and electrochemical behavior.

Overall, this study demonstrates that precise nanoparticle size and morphology optimization using DLS plays a crucial role in enhancing the electrochemical performance of ZnS-CoS electrodes. The optimized ZnS-CoS nanoparticles not only surpass many previously reported transition metal sulfide-based electrodes but also establish a new benchmark for next-generation supercapacitor materials. The combination of high capacitance, superior energy and power density, excellent stability, and favorable charge storage kinetics makes ZnS-CoS a highly promising candidate for high-performance energy storage devices. Future research can explore further material modifications, hybrid structures, and scalable synthesis approaches to enable the widespread adoption of ZnS-CoS for commercial supercapacitor applications.

View Article Online
DOI: 10.1039/D5MA00846H

Supporting Information

The supporting information of this article contains synthesis and characterization of ZnS and CoS nanoparticles, temperature-based optimization, pH-based optimization, reagent time of addition-based optimization, and stabilizer concentration-based optimization. It also includes comparison between experimental results and RSM, TPOT, and ANN model predictions at different scan rates.

Competing interests

The authors declare that they have no competing interests.

Author's contributions

Hafeez Ur Rehman: Benchwork, characterization, and initial draft preparation. Hamza Khan: Computational analysis, reviewing and editing. Zeeshan Abbasi and Amir Waseem: Characterization. Lotfi Ben Tahar: Funding and reviewing. Rafaqat Ali Khan: Electrochemical analysis. Ahson Jabbar Shaikh: Conceptualization, Visualization, Methodology, Investigation, Supervision, Writing, Reviewing, Editing, and Validation. All authors read and approved of the final manuscript.

Acknowledgments (Funding)

The authors extend their appreciation to the Deanship of Scientific Research at Northern Border University, Arar, KSA, for funding this research work through the project number "NBU-FFR-2025-2482-04".

Author information

*AJS, PhD; corresponding author; Cell: +92-(0)334-377-0104; Fax: +92-(0)992-383-441

Data availability

Data sharing is not applicable to this article as no datasets were generated or analyzed during the current study.

References

1. Alami, A.H., *Mechanical energy storage for renewable and sustainable energy resources*. 2020: Springer.
2. Olabi, A.G., et al., *Critical review of energy storage systems.* Energy, 2021. **214**: p. 118987.

View Article Online
DOI: 10.1039/D5MA00846H

3. Gao, Y. and L. Zhao, *Review on recent advances in nanostructured transition-metal-sulfide-based electrode materials for cathode materials of asymmetric supercapacitors.* Chemical Engineering Journal, 2022. **430**: p. 132745.
4. Ahmad, S.A., et al., *CoSe2@ ZnS microsphere arrays with remarkable electrochemical performance for hybrid asymmetric supercapacitor.* Journal of Energy Storage, 2023. **73**: p. 109090.
5. Barik, R. and P.P. Ingole, *Challenges and prospects of metal sulfide materials for supercapacitors.* Current Opinion in Electrochemistry, 2020. **21**: p. 327-334.
6. Khan, H., et al., *Tailoring hydrodynamic size and stability of TiO2–SiO2 nanoparticles for enhanced electrochemical performance of supercapacitors.* Materials Chemistry and Physics, 2026. **347**: p. 131423.
7. Iqbal, M.Z., M.M. Faisal, and S.R. Ali, *Integration of supercapacitors and batteries towards high-performance hybrid energy storage devices.* International Journal of Energy Research, 2021. **45**(2): p. 1449-1479.
8. Rui, X., H. Tan, and Q. Yan, *Nanostructured metal sulfides for energy storage.* Nanoscale, 2014. **6**(17): p. 9889-9924.
9. Rashid Khan, H. and A. Latif Ahmad, *Supercapacitors: Overcoming current limitations and charting the course for next-generation energy storage.* Journal of Industrial and Engineering Chemistry, 2025. **141**: p. 46-66.
10. Das, A., et al., *Performance and future directions of transition metal sulfide-based electrode materials towards supercapacitor/supercapattery.* WIREs Energy and Environment, 2022. **11**(1): p. e414.
11. Pazhamalai, P., et al., *Copper tungsten sulfide anchored on Ni-foam as a high-performance binder free negative electrode for asymmetric supercapacitor.* Chemical Engineering Journal, 2019. **359**: p. 409-418.
12. Hussain, I., et al., *Different controlled nanostructures of Mn-doped ZnS for high-performance supercapacitor applications.* Journal of Energy Storage, 2020. **32**: p. 101767.
13. Gan, Y., et al., *Trumpet-Like ZnS@ C Composite for High-Performance Potassium Ion Battery Anode.* Chemistry–A European Journal, 2023. **29**(32): p. e202300373.
14. Li, Z., et al., *Flaky CoS 2 and graphene nanocomposite anode materials for sodium-ion batteries with improved performance.* RSC advances, 2016. **6**(74): p. 70632-70637.
15. Ma, T., et al., *Nickel-cobalt-molybdenum sulfides with adjustable morphology via coprecipitation and hydrothermal conversion as high-performance electrodes for asymmetric supercapacitors.* Journal of Alloys and Compounds, 2020. **838**: p. 155631.
16. Venkateshalu, S., D. Rangappa, and A.N. Grace, *Hydrothermal synthesis and electrochemical properties of CoS2–reduced graphene oxide nanocomposite for supercapacitor application.* International Journal of Nanoscience, 2018. **17**(01n02): p. 1760020.
17. Chen, W., C. Xia, and H.N. Alshareef, *One-step electrodeposited nickel cobalt sulfide nanosheet arrays for high-performance asymmetric supercapacitors.* ACS nano, 2014. **8**(9): p. 9531-9541.
18. Gao, M.-R., et al., *Nanostructured metal chalcogenides: synthesis, modification, and applications in energy conversion and storage devices.* Chemical Society Reviews, 2013. **42**(7): p. 2986-3017.
19. Liu, Y., et al., *Design, synthesis, and energy-related applications of metal sulfides.* Materials Horizons, 2016. **3**(5): p. 402-421.
20. Li, H., et al., *Zinc cobalt sulfide nanoparticles as high performance electrode material for asymmetric supercapacitor.* Electrochimica Acta, 2019. **319**: p. 716-726.

View Article Online
DOI: 10.1039/D5MA00846H

21. Du, N., et al., *Nanosheet-assembled NiS hollow structures with double shells and controlled shapes for high-performance supercapacitors.* Chemical Engineering Journal, 2017. **323**: p. 415-424.
22. Shafaat, S., et al., *Understanding adsorption phenomena through dynamic light scattering and stability measurements.* International Journal of Environmental Analytical Chemistry, 2025: p. 1-22.
23. Afzal, M.Y., et al., *Understanding Photocatalytic Degradation of RB5 Dye under Salts Using Nickel Sulfide Nanoparticles: Insights from Dynamic Light Scattering and Theoretical Investigations.* ACS Omega, 2025.
24. Li, H., et al., *Electrochemical performance of LiNi 0.5 Mn 0.5 O 2 with different synthesis methods.* Rare Metals, 2015. **34**: p. 580-585.
25. Dong, H., A. Wang, and G.M. Koenig Jr, *Role of coprecipitation and calcination of precursors on phase homogeneity and electrochemical properties of battery active materials.* Powder Technology, 2018. **335**: p. 137-146.
26. Valenzuela, M., et al., *Comparison between sol-gel, coprecipitation and wet mixing synthesis of ZnAl2O4.* Journal of Sol-Gel Science and Technology, 1997. **8**(1): p. 107-110.
27. Rai, R., S. Alwani, and I. Badea, *Polymeric nanoparticles in gene therapy: New avenues of design and optimization for delivery applications.* Polymers, 2019. **11**(4): p. 745.
28. Do Kim, K., et al., *Optimization of parameters for the synthesis of zinc oxide nanoparticles by Taguchi robust design method.* Colloids and Surfaces A: Physicochemical and Engineering Aspects, 2007. **311**(1-3): p. 170-173.
29. Nemade, K. and S. Waghuley, *Ultra-violet C absorption and LPG sensing study of zinc sulphide nanoparticles deposited by a flame-assisted spray pyrolysis method.* Journal of Taibah University for Science, 2016. **10**(3): p. 437-441.
30. Saleem, A., et al., *The synergistic effect of electron lone pairs and aromaticity on the binding affinity towards metal surfaces.* Colloids and Surfaces A: Physicochemical and Engineering Aspects, 2023. **664**: p. 131127.
31. Xu, J., et al., *One-step electrodeposition fabrication of Ni3S2 nanosheet arrays on Ni foam as an advanced electrode for asymmetric supercapacitors.* SCIENCE CHINA-MATERIALS, 2019. **62**(5): p. 699-710.
32. Saeed, W., et al., *Interactive behavior of graphene quantum dots towards noble metal surfaces.* Physica E: Low-dimensional Systems and Nanostructures, 2023. **147**: p. 115596.
33. Huang, G., F. Huang, and W. Dong, *Machine learning in energy storage material discovery and performance prediction.* Chemical Engineering Journal, 2024: p. 152294.
34. Lu, Z., *Computational discovery of energy materials in the era of big data and machine learning: a critical review.* Materials Reports: Energy, 2021. **1**(3): p. 100047.
35. Tawfik, W.Z., et al., *An artificial neural network model for capacitance prediction of porous carbon-based supercapacitor electrodes.* Journal of Energy Storage, 2023. **73**: p. 108830.
36. Lu, X., et al., *Research on prediction of energy density and power density of biomass carbon-based supercapacitors based on machine learning.* Sustainable Materials and Technologies, 2025. **44**: p. e01309.
37. Liu, C., Q. Li, and K. Wang, *State-of-charge estimation and remaining useful life prediction of supercapacitors.* Renewable and Sustainable Energy Reviews, 2021. **150**: p. 111408.
38. Shaikh, A.J., et al., *Plasmonic Effects, Size and Biological Activity Relationship of Au-Ag Alloy Nanoparticles.* Journal of Nano Research, 2018. **54**: p. 98-111.
39. Ullah, M., et al., *Sustainable graphitic carbon derived from oil palm frond biomass for supercapacitor application: Effect of redox additive and artificial neural network-based modeling approach.* 2024. **971**: p. 118570.

View Article Online
DOI: 10.1039/D5MA00846H

40. Tawfik, W.Z., et al., *Insights into the specific capacitance of CNT-based supercapacitor electrodes using artificial intelligence.* 2025. **15**(5): p. 3155-3167.
41. Reddy, B., et al., *Modeling capacitance of carbon-based supercapacitors by artificial neural networks.* 2023. **72**: p. 108537.
42. Ebied, M.A., M.A. Azim, and A.J.J.o.E.S. Emad-Eldeen, *AI-based approach for predicting the storage performance of zinc oxide-based supercapacitor electrodes.* 2024. **94**: p. 112292.
43. Dongale, T., et al., *Development of nano fiber MnO2 thin film electrode and cyclic voltammetry behavior modeling using artificial neural network for supercapacitor application.* 2015. **36**: p. 43-48.
44. Liu, P., et al., *New insights into the performance of biomass carbon-based supercapacitors based on interpretable machine learning approach.* 2025. **118**: p. 116300.
45. Bu, R., et al., *"One-for-two" strategy: the construction of high performance positive and negative electrode materials via one Co-based metal organic framework precursor for boosted hybrid supercapacitor energy density.* 2022. **541**: p. 231689.
46. Zhang, J., et al., *Chemically coupled 0D-3D hetero-structure of Co9S8-Ni3S4 hollow spheres for Zn-based supercapacitors.* 2022. **430**: p. 132836.
47. Bhattacharjee, S., *DLS and zeta potential–what they are and what they are not?* Journal of controlled release, 2016. **235**: p. 337-351.
48. Kasture, M., et al., *Synthesis of silver nanoparticles by sophorolipids: Effect of temperature and sophorolipid structure on the size of particles.* Journal of Chemical Sciences, 2008. **120**: p. 515-520.
49. Diwakar, B., et al., *Carboxymethyl cellouse stabilized cobalt sulfide nanoparticles: preparation, characterization and application.* Journal of Cluster Science, 2023. **34**(5): p. 2429-2439.
50. Amir, D., et al. *Effect of Stabilizers in the Synthesis of Silver Nanoparticles and Methylene Blue Oxidation*. in *IOP Conference Series: Materials Science and Engineering*. 2021. IOP Publishing.
51. de Santana, Y.V., et al., *Experimental and theoretical studies on the enhanced photoluminescence activity of zinc sulfide with a capping agent.* Journal of Applied Physics, 2011. **110**(12).
52. Senapati, U. and D. Sarkar, *Synthesis and characterization of biopolymer protected zinc sulphide nanoparticles.* Superlattices and Microstructures, 2015. **85**: p. 722-733.
53. Muradov, M.B., et al., *Synthesis and characterization of cobalt sulfide nanoparticles by sonochemical method.* Infrared Physics & Technology, 2018. **89**: p. 255-262.
54. Abza, T., et al., *Characterization of cobalt sulfide thin films synthesized from acidic chemical baths.* Advances in Materials Science and Engineering, 2020. **2020**(1): p. 2628706.
55. Ait-karra, A., et al., *Effect of hydrothermal temperature on the structural, morphological, optical properties and photocatalytic performances of cobalt sulfide nanomaterials.* Journal of Alloys and Compounds, 2024. **999**: p. 174946.
56. Zhang, Y., et al., *Coupling of heterogeneous advanced oxidation processes and photocatalysis in efficient degradation of tetracycline hydrochloride by Fe-based MOFs: Synergistic effect and degradation pathway.* Chemical Engineering Journal, 2019. **369**: p. 745-757.
57. Ramachandran, R., et al., *Synthesis of cobalt sulfide–graphene (CoS/G) nanocomposites for supercapacitor applications.* IEEE transactions on nanotechnology, 2013. **12**(6): p. 985-990.

View Article Online
DOI: 10.1039/D5MA00846H

58. Aftab, J., et al., *Synergetic electrochemical performance of tungsten oxide/tungsten disulfide/MWCNTs for high-performance aqueous asymmetric supercapattery devices.* Journal of Alloys and Compounds, 2023. **965**: p. 171366.
59. Zhao, J., et al., *Multilayer dodecahedrons Zn-Co sulfide for supercapacitors.* Electrochimica Acta, 2020. **354**: p. 136714.
60. Imran, M., et al., *Designing of WS2@ NiCoS@ ZnS nanocomposite electrode material for high-performance energy storage applications.* Crystals, 2024. **14**(11): p. 916.
61. Ravisankar, D., et al., *Novel Surface-Enriched Spiky Ball With Spines NiCo2S4@ GO/CNT Electrode Material for a High-Performance Flexible Asymmetric Supercapacitor.* ECS Journal of Solid State Science and Technology, 2024. **13**(1): p. 011001.
62. Miya, L.A., et al., *Eco-friendly and sustainable supercapacitor design: Cobalt sulfide nanoparticles embedded on carbon cloth as an electrode material for asymmetric devices.* 2025: p. 1-15.
63. Ashok Kumar, K., et al., *Effect of bi-functional hierarchical flower-like CoS nanostructure on its interfacial charge transport kinetics, magnetic and electrochemical behaviors for supercapacitor and DSSC applications.* 2019. **9**(1): p. 1228.
64. Zhou, W., et al., *CoS x/C hierarchical hollow nanocages from a metal–organic framework as a positive electrode with enhancing performance for aqueous supercapacitors.* 2019. **9**(20): p. 11253-11262.
65. Zainab, S., et al., *Exploring electrolyte specific effects on multisheets 2-dimensional Ti3C2Tx-BiFeO3 nanocomposites electrodes for high-performance supercapacitors applications.* 2025. **15**(1): p. 22848.
66. Iqbal, M.Z., U. Abbasi, and M. Alzaid, *Cobalt manganese phosphate and sulfide electrode materials for potential applications of battery-supercapacitor hybrid devices.* Journal of Energy Storage, 2022. **50**: p. 104632.
67. Vijayakumar, S., et al., *Facile synthesis of Zn-Co-S nanostrip cluster arrays on Ni foam for high-performance hybrid supercapacitors.* Nanomaterials, 2021. **11**(12): p. 3209.
68. Ahmad, R., et al., *Zeolitic imidazolate frameworks derived Co-Zn-nanoporous carbon-sulfide material for supercapacitors.* Electrochimica Acta, 2022. **404**: p. 139739.
69. Zang, X., et al., *Solvent-Controlled Morphology of Zinc–Cobalt Bimetallic Sulfides for Supercapacitors.* Molecules, 2023. **28**(18): p. 6578.
70. Rakhi, R., et al., *Nanostructured cobalt sulfide-on-fiber with tunable morphology as electrodes for asymmetric hybrid supercapacitors.* Journal of Materials Chemistry A, 2014. **2**(38): p. 16190-16198.
71. Rauf, M., et al., *Facile hydrothermal synthesis of zinc sulfide nanowires for high-performance asymmetric supercapacitor.* Journal of Saudi Chemical Society, 2022. **26**(4): p. 101514.
72. De, P., et al., *Role of porosity and diffusion coefficient in porous electrode used in supercapacitors–Correlating theoretical and experimental studies.* Electrochemical Science Advances, 2023. **3**(1): p. e2100159.
73. Afzal, A.M., et al., *Exploring the redox characteristics of porous ZnCoS@ rGO grown on nickel foam as a high-performance electrode for energy storage applications.* RSC advances, 2023. **13**(31): p. 21236-21248.
74. Gao, Y., et al., *Double metal ions synergistic effect in hierarchical multiple sulfide microflowers for enhanced supercapacitor performance.* ACS applied materials & interfaces, 2015. **7**(7): p. 4311-4319.
75. Li, T., et al., *Predicting high-strength concrete's compressive strength: a comparative study of artificial neural networks, adaptive neuro-fuzzy inference system, and response surface methodology.* 2024. **17**(18): p. 4533.

76. Desalegn, Y.M., et al., *RSM versus ANN for modeling and optimization of magnetic adsorbent based on montmorillonite and CoFe2O4.* 2024. **14**(6): p. 129.
77. Khoshraftar, Z., A. Ghaemi, and A.J.S.R. Hemmati, *Comprehensive investigation of isotherm, RSM, and ANN modeling of CO2 capture by multi-walled carbon nanotube.* 2024. **14**(1): p. 5130.
78. Luan, W., et al., *Optimization of a polyvinyl butyral synthesis process based on response surface methodology and artificial neural network.* 2023. **13**(11): p. 7682-7693.
79. Ahmad, S.A., et al., *Facile synthesis of hierarchical ZnS@ FeSe2 nanostructures as new energy-efficient cathode material for advanced asymmetric supercapacitors.* 2022. **7**(4): p. 100489.
80. Ahmad, S.A., et al., *High power aqueous hybrid asymmetric supercapacitor based on zero-dimensional ZnS nanoparticles with two-dimensional nanoflakes CuSe2 nanostructures.* 2023. **49**(12): p. 20007-20016.
81. Yu, F., et al., *Flower-like Cu5Sn2S7/ZnS nanocomposite for high performance supercapacitor.* 2019. **30**(5): p. 1115-1120.

The data supporting this article have been included as part of the Supplementary Information.

View Article Online
DOI: 10.1039/D5MA00846H